

Lattice Boltzmann Approach for Local Reference Frames

Raoyang Zhang*, Chenghai Sun, Yanbing Li, Rajani Satti,
Richard Shock, James Hoch and Hudong Chen

EXA Corporation, 55 Network Drive, Burlington, MA 01803, USA.

Received 2 November 2009; Accepted (in revised version) 11 November 2010

Available online 28 January 2011

Abstract. In this paper we present a generalized lattice Boltzmann based approach for sliding-mesh local reference frame. This scheme exactly conserves hydrodynamic fluxes across local reference frame interface. The accuracy and robustness of our scheme are demonstrated by benchmark validations.

PACS: 47.11.Qr, 44.05.+e

Key words: LBM, LRF, sliding mesh.

1 Introduction

The fluid flows associated with rotating systems are quite complex and are characterized by a variety of unsteady flow phenomena such as laminar-turbulent transitions, boundary layer separation and reattachment, formation and evolution of vortices and above all, mixing and entrainment processes. Such flows are found in almost every industrial process involving fans, propellers, blowers, pumps, stirred tanks, turbo machinery components etc. Although experiments [1, 2] are commonly conducted to understand the complex physics of rotating systems, they are generally expensive, time consuming and can only provide limited data.

Computational modeling of moving geometry across grids is generally difficult and expensive. However, for certain types of motions, such as rotation, one may come up with substantial simplifications. For simulation of flow with arbitrary geometry that is rotating in time around a fixed axis, a rotating fan for example, the three dimensional computational domain can be divided into an inner domain and outer domain. The inner domain has its grid fixed with the rotating geometry so that the geometry does not have a relative motion with respect to the grid. This forms a local reference frame (LRF) domain "body-fixed" with the rotating geometry. The grid in the outer domain

*Corresponding author. *Email addresses:* raoyang@exa.com (R. Zhang), chenghai@exa.com (C. Sun), leolee@exa.com (Y. Li), Rajani.Satti@bakerhughes.com (R. Satti), rshock@exa.com (R. Shock), hoch@exa.com (J. Hoch), hudong@exa.com (H. Chen)

is fixed with the ground and forms a "ground-fixed" reference frame domain. Between the inner domain and outer domain, there is a closed transparent interface to connect fluid flows. Since there is no relative motion between geometry and its neighboring grid, the difficulty in treating moving geometry can be avoided. The relative motion only exists on the interface between the inner and outer grids. Because the interface has an axisymmetric shape with the axis coinciding with the rotational axis, the relative motion is only tangential, i.e., sliding, and no deformation to either domain occurs. This so-called "sliding mesh" interface should only serve for computational purpose and should not disturb the flow across it. The fluxes across the boundary from body fixed to ground fixed frames and vice versa, including mass flux, momentum flux and heat flux etc, should be conserved. This requires a nontrivial matching between two domains at the vicinity of the interface.

The general idea of matching a rotating grid with a non-rotating one is not new. In conventional Navier-Stokes based CFD, an axisymmetric volume mesh near such a sliding mesh interface is usually used on inner and outer sides. This could be an extra constraint on mesh generation. Various numerical interpolations are also needed to match fluid flows across the sliding mesh boundary. The task becomes significantly more difficult if non axisymmetric mesh such as Cartesian mesh is used. It would require expensive computation of time varying weights that link the inner and outer grid points everywhere along the vicinity of the sliding mesh boundary. This could also seriously compromise accuracy of numerical solutions in terms of ensuring conservation laws. Many conventional methods of sliding mesh can be found in literature. One early example is the work of Murthy et al. [3, 4], whereby a sliding mesh technique was developed for time-dependent simulation of the flow in mixing tanks. Later studies by Tabor et al. [5] and Dasakapoulos and Harris [6] further explored the applicability of traditional sliding mesh methodology for mixing tanks and Rushton impeller stirred tanks.

The kinetic-theory based lattice Boltzmann method (LBM) is a well-known CFD approach for transient, viscous flow simulation that involves complex fluid phenomena [7]. LBM describes fluid flow in terms of a discrete kinetic equation for particle density distribution functions, namely the lattice Boltzmann equation (LBE). The macroscopic flow properties are direct results of the moments of these particle distribution functions. At the hydrodynamic limit it has been shown that the LBE recovers the Navier-Stokes equation [8, 9]. It has also been demonstrated recently that through a moment expansion procedure, LBE can be extended to describe fluid dynamics beyond Navier-Stokes hydrodynamics [10–12].

LBM has many advantages over traditional CFD [7], particularly, the straightforward boundary condition implementation enables flow simulation on a Cartesian grid system while maintaining exact conservations [13]. This makes LBM very convenient for accurately handling flow that involves complex geometry. Because of its kinetic nature, it is also easy and more physical to model various complex fluid flows [7, 14]. Furthermore, the unsteady Very-Large-Eddy-Simulation (VLES) turbulence model has been incorporated successfully into LBM [15, 16]. Its numerical accuracy and robustness have been

widely demonstrated and validated in scientific research as well as in real engineering applications [7, 17, 18]. Since rotating flows associated with LRF are usually highly unsteady and require delicate handling of LRF interface, it is not surprising that LBM has an advantage to deal with sliding mesh problems.

In this study, we present a complete LB based sliding mesh algorithm for rotating fluid flow system and demonstrate its accuracy, robustness and capability in benchmark validations. The paper is organized as follows: in the next sections, we first provide a detailed description of the numerical scheme, then present three sets of numerical results to validate the scheme and conclude at last.

2 Numerical algorithm

The basic sliding mesh lattice Boltzmann concept and algorithm for solving fluid flows across different reference frames were formulated by Chen and Hoch in 2004 and 2005. Inside each reference frame, the fluid flow is solved by the most commonly used D3Q19 LB-BGK model [9] with an external body force:

$$f_i(\mathbf{x} + \mathbf{c}_i, t + 1) = f_i(\mathbf{x}, t) - \frac{1}{\tau} (f_i(\mathbf{x}, t) - f_i^{eq}(\mathbf{x}, t)) + \mathbf{F}_i(\mathbf{x}, t).$$

Here $f_i(\mathbf{x}, t)$ is the particle density distribution function and τ is the so-called single relaxation time. The equilibrium distribution function $f_i^{eq}(\mathbf{x}, t)$ has the following 3rd order form:

$$f_i^{eq}(\mathbf{x}, t) = \rho \omega_i \left(1 + \frac{\mathbf{c}_i \cdot \mathbf{u}}{T_0} + \frac{(\mathbf{c}_i \cdot \mathbf{u})^2}{2T_0^2} - \frac{\mathbf{u}^2}{2T_0} + \frac{(\mathbf{c}_i \cdot \mathbf{u})^3}{6T_0^3} - \frac{(\mathbf{c}_i \cdot \mathbf{u})\mathbf{u}^2}{2T_0^2} \right)$$

with $\omega_0 = 1/3$ for stop state, $\omega_i = 1/12$ for states in Cartesian directions and $\omega_i = 1/36$ for states in bi-diagonal directions. Here $T_0 = 1/3$ is the constant lattice temperature. The hydrodynamic quantities ρ and $\rho \mathbf{u}$ are the zeroth and first order moments of the distribution functions respectively:

$$\rho(\mathbf{x}, t) = \sum_i f_i(\mathbf{x}, t), \quad \rho(\mathbf{x}, t) \mathbf{u}(\mathbf{x}, t) = \sum_i \mathbf{c}_i f_i(\mathbf{x}, t).$$

The external body force $\mathbf{F}_i(\mathbf{x}, t)$ corresponds to the inertial force $\mathbf{A}(\mathbf{x}, t)$ introduced by the non-inertial rotating LRF:

$$\mathbf{A}(\mathbf{x}, t) = -\Omega(t) \times (\Omega(t) \times \mathbf{r}(\mathbf{x}, t)) - 2\Omega(t) \times \mathbf{u}'(\mathbf{x}, t) - \frac{d\Omega(t)}{dt} \times \mathbf{r}(\mathbf{x}, t).$$

The $\Omega(\mathbf{x}, t)$ is the rotational angular velocity of the LRF and the $\mathbf{r}(\mathbf{x}, t)$ is the distance vector from the origin point of LRF to the fluid position. $\mathbf{u}(\mathbf{x}, t)$ is the local pre-collide fluid velocity seen in the non-inertial LRF defined above. The fluid velocity in f_i^{eq} is equal to the pre-collide $\mathbf{u}(\mathbf{x}, t)$ shifted by $\mathbf{A}(\mathbf{x}, t)/2$:

$$\mathbf{u}'(\mathbf{x}, t) = \mathbf{u}(\mathbf{x}, t) + \frac{\mathbf{A}(\mathbf{x}, t)}{2},$$

the external body force has the following form [19]:

$$\mathbf{F}_i = \left(1 - \frac{1}{2\tau}\right) \rho \omega_i \left(\frac{(\mathbf{c}_i - \mathbf{u}') \cdot \mathbf{A}}{T_0} + \frac{(\mathbf{c}_i \cdot \mathbf{u}')(\mathbf{c}_i \cdot \mathbf{A})}{T_0^2} \right).$$

It is worth pointing out that such a body force treatment has a second order accuracy in velocity space and is essential to the accuracy of numerical simulations in LRF.

The most challenging part of simulating flows across different reference frames is the flow transition across the sliding mesh boundary. To allow smooth and accurate information exchange across the boundary, we first separate the LRF region from the ground fixed region by introducing cylindrical double layered transparent surfaces. Indeed, any rotational-axisymmetric surface is applicable here. Instead of direct matching between inner and outer grids, flow transition is realized dynamically between the inner and outer surface boundaries. The inner surface boundary is fixed with the inner Cartesian grids and the outer surface boundary is fixed with the outer ones. Each of the cylindrical surfaces is then divided into m sets of rings orthogonal to the LRF rotational axis. Each ring surface is made of a set of surface elements of the same size within the ring. The surface elements within each ring have the same shape since the ring surface is axisymmetric. There is no gap between the inner and outer surfaces, so that the outer surface elements have the same size and shape as the inner ones. The only difference between the inner and outer surfaces is that inner surface is facing the inner domain while the outer surface is facing the outer domain.

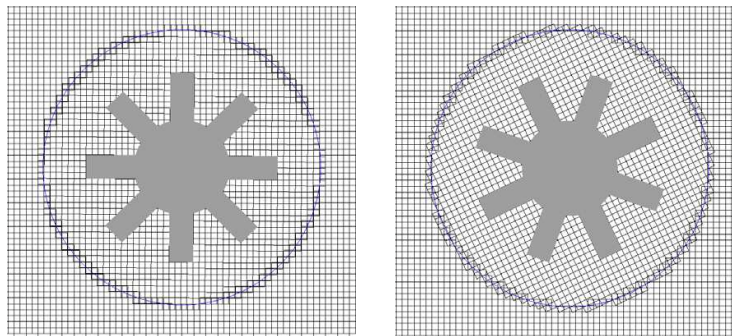


Figure 1: Schematic showing the sliding mesh grid at time, $t=0$ (left) and at a later time (right). Note that the rotating geometry is shown in grey and the sliding mesh interface is shown in blue.

Since the inner grids and the associated LRF boundary surface, i.e., the inner surface, are rotating while the outer ones are not, it results in a relative sliding motion between the two surfaces. Note there is no relative motion between grids and the associate LRF boundary, their geometrical weights are time independent and can be determined before simulation (see Fig. 1). The only calculation needed during simulation is the matching between inner and outer surface elements. Because of the identical size and shape for surface elements inside a given ring, each surface element on one side intercepts at most

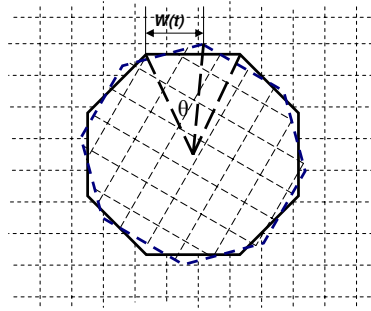


Figure 2: Illustration of matching of surface elements on sliding mesh boundary. The solid lines represent outer LRF surface and the dashed lines represent the rotating inner sliding mesh surface. θ is the rotating angle and $\omega(t)$ is the matching ratio.

two surface elements on the other side at any given time (Fig. 2). There is only one matching ratio $\omega(t)$ for all surface elements in each ring:

$$\omega(t) = \frac{|A^{out} \cap A^{in}|}{|A|}, \quad |A^{out}| = |A^{in}| = |A|,$$

where $A(A^{in}, A^{out})$ represents a surface (inner, outer) element on a ring, and $|A|$ is its area. Here ω is LRF rotating angle θ dependent and $0 \leq \omega < 1$. For each inner or outer surface element, it receives ω part of flow information from one matched surface element and $(1-\omega)$ part from the other matched one on the other side. Since ω is a scalar and only needs to be calculated once for each ring at each time step, its computational cost is minimum. In addition, matching of surface elements can be easily realized in real operations by an indicator. Therefore the total computational cost of matching of surface elements due to LRF sliding motion is tiny. For the purpose of simplicity in geometry discretization, planar surface elements shown in Fig. 2 are used in current study. Their approximation to a circular ring improves as more but smaller flat elements are used.

The standard gather and scatter scheme on surface element can be directly performed on both sides. The original concept and scheme of frictionless boundary condition, including details in surface scattering and gathering, on arbitrary geometries were formulated by Chen et al. in 1998 (see [13]). This approach exactly conserves local mass and surface tangential momentum fluxes while reflecting the normal momentum flux. It also satisfies the local detailed balance. This boundary scheme can be extended naturally to treat flow transition across LRF boundaries, so that both the normal and tangential momentum fluxes are conserved. The following are the detailed steps (c.f. [13]):

1. Gather incoming states and sample mass and momentum from neighbor cells on both sides of LRF surfaces.
2. Match LRF surface elements between outer and inner surfaces. As mentioned earlier, each surface element on one side communicates with two surface elements on the other side at any given time. The matching ratio of two surface elements depends on the LRF rotational position.

3. Transform the surface velocity from LRF to ground fixed reference frame on LRF side.
4. Calculate averaged values of mass $\bar{\rho}$ and momentum $\bar{\rho}\bar{\mathbf{u}}$ for each matched LRF surface element pairs in ground fixed reference frame. Then the momentum $\bar{\rho}\bar{\mathbf{u}}_{LRF}$ values in LRF are also calculated.
5. Construct $f_i^{eq}(\bar{\rho}, \bar{\rho}\bar{\mathbf{u}})$ on surface element in ground fixed reference frame and $f_i^{eq}(\bar{\rho}, \bar{\rho}\bar{\mathbf{u}}_{LRF})$ on surface element in LRF.
6. Apply the same surface collision rules in all surface elements as in [13].
7. Add proper skin friction τ_ω according to local fluid viscous dissipation.
8. Ensure local mass conservation as in [13].
9. Scatter outgoing states back to neighbor cells.

Note that the surface velocity used in equilibrium calculation is a full velocity instead of the surface tangential velocity [13]. It can be shown rigorously that such an extended surface scheme conserves the mass and total momentum fluxes across LRF boundaries. The satisfaction of flux conservations is essential to realization of accurate and smooth transitions. The modified scheme of surface states scattering was proposed in [20] and has been demonstrated extensively to achieve second order numerical accuracy. Since many operational details, including gather and scatter procedure, surface collision rules and mass conservation assurance, are exactly the same as those in [13, 20], we will not repeat them in this paper.

The LBM boundary conditions for solid walls used in this paper are again the same as those described in [13]. It should be noted that a rotating solid wall in the ground fixed reference frame becomes a static wall in the LRF. This is indeed one of the original purposes of LRF.

So far we have presented a complete LB scheme for LRF. For most of the engineering applications, turbulence modeling is inevitable. The most common approach is to solve partial differential equations (PDE) for turbulent kinetic energy κ and turbulent dissipation ε to compute an eddy viscosity ν_{eddy} [21]. The turbulence model we used in this paper is the VLES model [15, 16, 21]. Since there are relative motions between reference frames, the interior mesh and exterior mesh are mismatched at most of the simulation time. The PDE can not be solved directly across the LRF boundaries. By employing a similar sliding mesh concept as discussed above for LB, the scalar flux across LRF boundaries due to scalar advection and diffusion of a scalar transport equation can be solved accurately and smoothly without involving complicated numerical interpolations. The detailed algorithm will be described in a separate paper.

3 Numerical validations

Based on the sliding mesh algorithm presented in the previous section for laminar/turbulent flows, time accurate numerical validations were conducted for three different cases: 2D

direct numerical simulation (DNS) of rotating Cylinder flow, 2D direct numerical simulation of cross flow past a single rotating blade and a 3D turbulent flow past a D4119 benchmark Propeller.

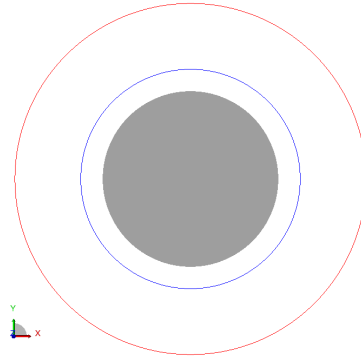


Figure 3: Schematic showing the test case of the rotating cylinder. Note that the grey region is the inner cylinder. Blue region indicates the sliding mesh interface and the red region corresponds to the stationary outer cylinder.

3.1 2D-DNS-Rotating cylinder

As a first test, a simple case of a 2D-DNS Rotating cylinder in Fig. 3 is considered to examine the accuracy of the scheme. The case consists of two cylinders with the inner cylinder rotating at a fixed velocity and the outer cylinder stationary. The fluid viscosity is 0.01 in lattice units for the case of resolution 16, and the corresponding τ is 0.53. The Reynolds number is 147 and the rotating angular velocity is 0.00573 radians per lattice time step. The sliding mesh interface (shown in blue) is specified at different distances from the rotating cylinder. We conducted simulations of various resolutions for two different cases corresponding, respectively, to the locations of sliding mesh interface with distances of $r/32$ and $r/2$ from the inner rotating cylinder, where r is the radius of the inner rotating cylinder. Figs. 4 and 5 show comparisons of tangential velocity normalized by the maximum velocity (the velocity value at the surface of inner rotating cylinder) between the simulations with and without sliding mesh for the two different cases at resolutions 16, 32 and 64, respectively. They show the gradual decay in velocity as we transverse from the rotating cylinder to the stationary cylinder. Figs. 6 and 7 show comparisons of pressure values. As seen from the plots, one can clearly infer that there is a smooth flow transition across the sliding mesh interface located at $r/32$ and $r/2$, indicating the accuracy of the simulation in such a stressful situation with low viscosity and coarse resolution. Both simulations also show very good resolution convergence. Fig. 8 shows the velocity errors measured by L_2 -norm verse simulation resolution. The error is defined as:

$$err = \frac{\sqrt{\sum_n |\mathbf{u}_n^{lrf} - \mathbf{u}_n^{no-lrf}|}}{N},$$

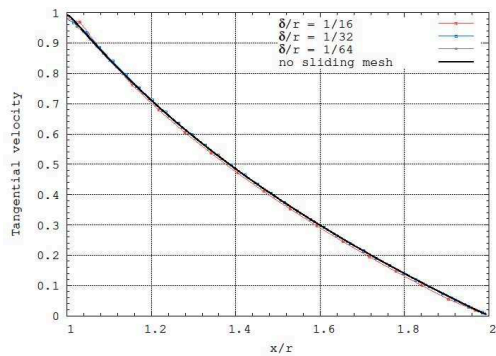


Figure 4: Comparisons of normalized velocity profiles of the $r/32$ case.

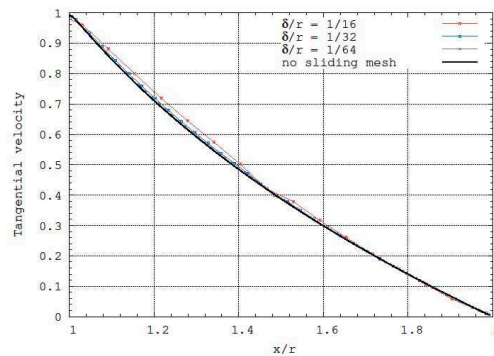


Figure 5: Comparisons of normalized velocity profiles of the $r/2$ case.

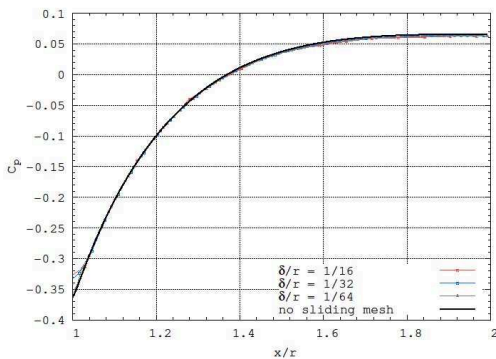


Figure 6: Comparisons of C_p profiles of the $r/32$ case.

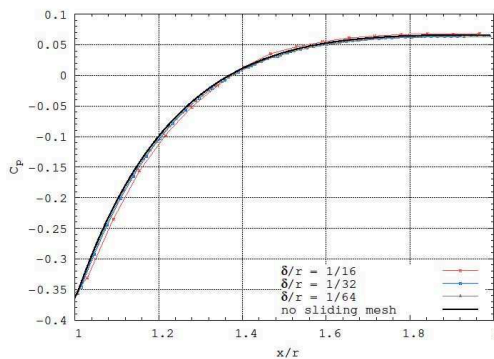


Figure 7: Comparisons of C_p profiles of the $r/2$ case.

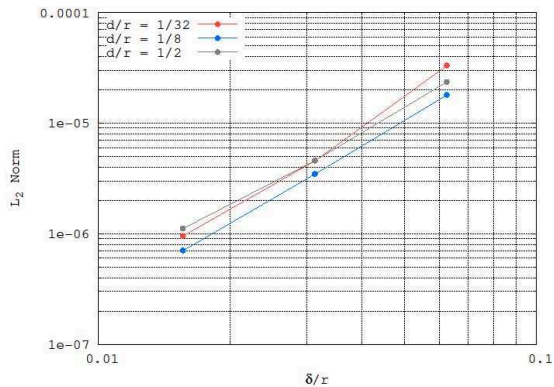


Figure 8: Velocity error measured by L_2 -norm verse resolution, d represents the sliding mesh distance from the rotating cylinder.

where N is the total number of cells. The nearly exponential decay rates of the errors further indicate that resolution convergence of our scheme is satisfactory. We also want to point out that the scheme is capable of achieving good results consistently even when the distance of sliding mesh interface to the solid wall is less than one cell.

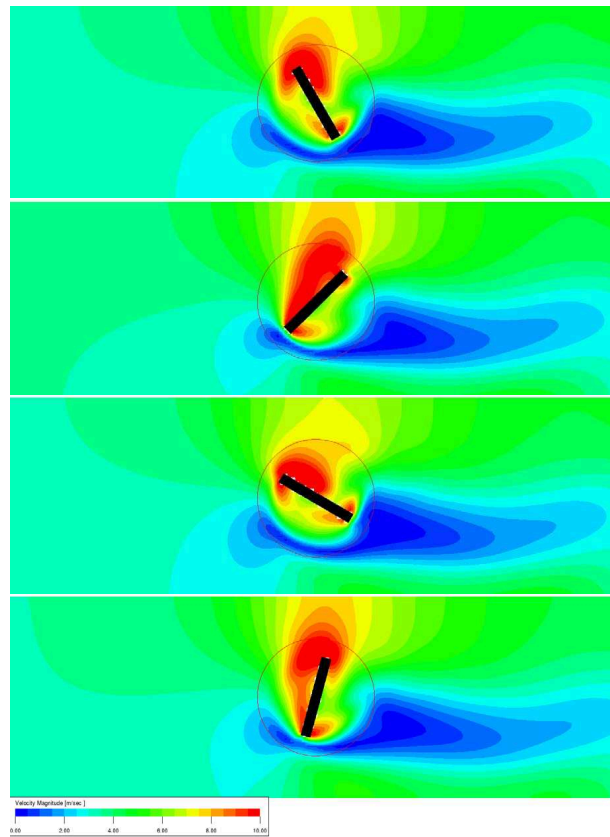


Figure 9: Snapshots of velocity magnitude for the 2D-DNS-Crossflow-Blade Case. The sliding mesh interface is highlighted as a red circular region.

3.2 2D-DNS-Blade in cross flow

To further ascertain the accuracy of the scheme, a rotating blade in a weak incoming flow is presented next. The Reynolds number is 115. The resolution across the blade is 32 and the rotating angular velocity is 0.0327 radians per lattice time step. Fig. 9 shows instantaneous snapshots of velocity magnitude at different blade angles as the sliding mesh region rotates. The rotating/sliding mesh interface is also indicated (in red color) in Fig. 9. As seen from the snapshots, the flow structure of the blade (maxima and minima of velocity) as it rotates is accurately captured by the current scheme. In addition, the smooth transition and the appropriate exchange of information across the interface are also indicated clearly in these images.

3.3 3D turbulent flow past D4119 Propeller

As the third and final validation test, a complex benchmark case of a propeller rotating in a uniform flow was chosen to demonstrate the capability of the sliding mesh algorithm

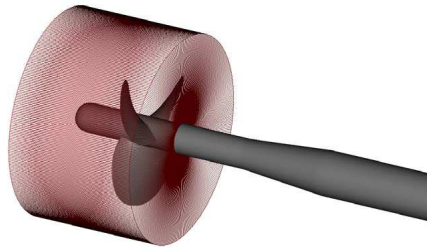


Figure 10: Schematic showing the sliding mesh region around the Propeller.

coupled with the turbulence solver. The typical Reynolds number for such a case is about 1.5×10^6 . The D4119 Propeller is a three bladed propeller designed in the 1960's to validate lifting surface design methods (Fig. 10). The Propeller was simulated with different advanced coefficients, $J = V/Nd$, where V is the advance velocity, n is the rotation speed (10rps) of the Propeller and R is the radius (152.4mm) of the Propeller. Our simulation results are compared directly with the experimental data of Jessup et al. [22]. More details about the Propeller geometry and experimental test conditions can be found in Jessup et al. [22].

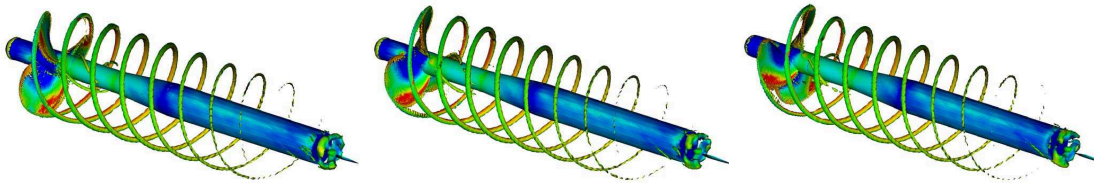


Figure 11: Instantaneous snapshots of surface pressure overlapped with isosurfaces of velocity magnitude for the Propeller case.

Fig. 10 shows illustration of the cylindrical sliding mesh surrounding the blade region of the Propeller. The LRF region is inside the cylindrical sliding mesh. The case is defined by 240 cells across the radius of the Propeller and is simulated in fully turbulent mode (LBM-VLES approach). Time accurate sliding mesh simulations coupled with the LBM-VLES approach were performed to test the accuracy and robustness of the current sliding mesh scheme. Fig. 11 shows snapshots of the flow around the Propeller at different time with surface pressure overlapped by λ_2 (colored by velocity), which is a vortex identification criteria proposed by Jeong and Hussain [23]. These images clearly demonstrate the complex rotationality of the flow and show smooth flow transition across LRF boundary.

Fig. 12 shows the comparisons of experiments/simulations for the Propeller efficiency, torque and thrust coefficients for various advance coefficients. The efficiency of the Propeller is well predicted at low advance coefficients with maximum under prediction shown at the peak efficiency point. The torque and thrust coefficients are in general well predicted for all advance coefficients.

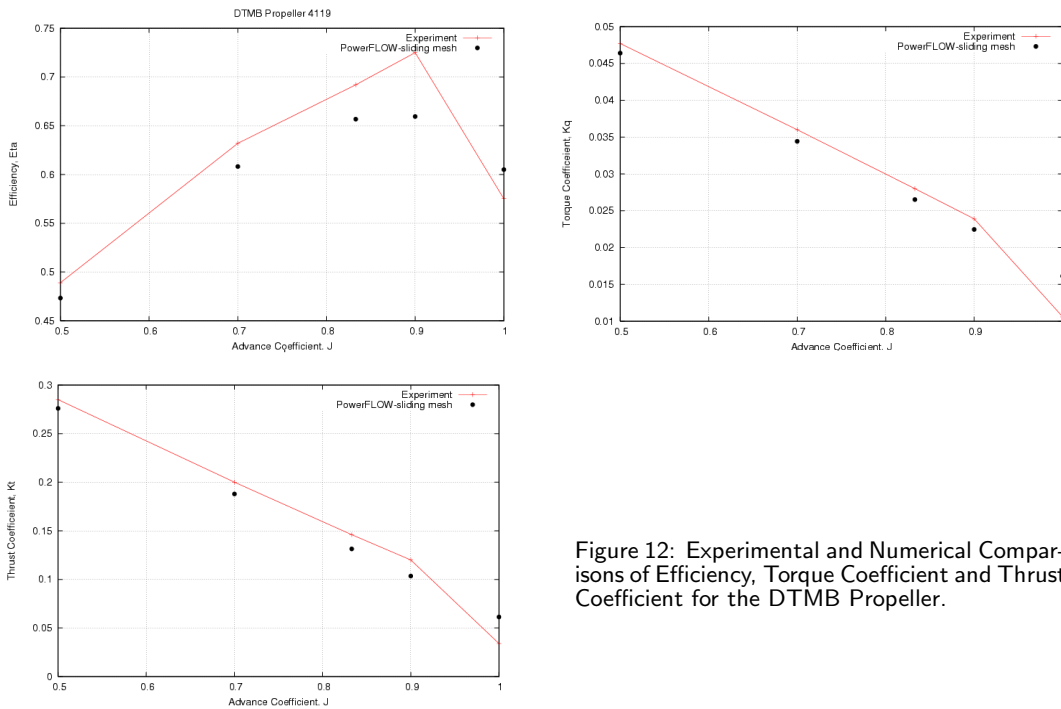


Figure 12: Experimental and Numerical Comparisons of Efficiency, Torque Coefficient and Thrust Coefficient for the DTMB Propeller.

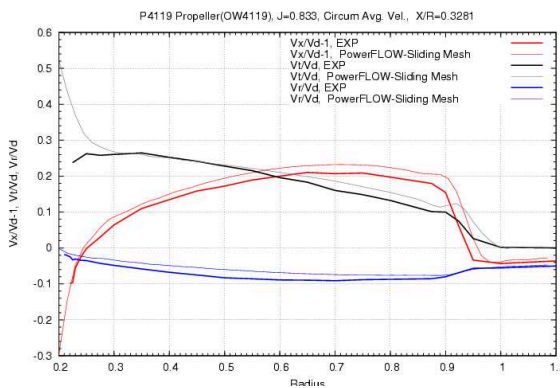


Figure 13: Circumferentially Averaged velocity component comparisons between experiments and simulations at a downstream Propeller location of $X/R = 0.3281$.

Fig. 13 shows comparisons of circumferentially averaged velocity components between the experiments and the LBM based sliding mesh simulations for the operating condition corresponding to $J = 0.833$. The velocities are compared downstream of the propeller at $X/R = 0.3281$, where X is positive downstream, with its origin at the propeller reference line. Note that all velocities are normalized by the advance speed V . The data in Fig. 13 is presented as line plots of velocity versus radius of the propeller. It shows good agreements with experimental data at all locations, although the axial velocity is slightly over predicted away from the center. Due to page limitation, other detailed results such as velocity distributions at downstream locations are not presented here.

4 Conclusions

In this paper, we presented a generalized LB based sliding mesh scheme for LRF. The LRF surface mesh is generated as standard solid wall without any special requirement. The surface dynamics and matching scheme of the LRF interface obey conservation laws so that the flow transition across the LRF boundary is accurate and robust. Since there is no need for expensive time dependent weights calculation, the whole computational cost of each LRF surface element is comparable to the cost of computing the standard static solid boundary. The algorithm can be parallelized easily and achieve almost linear scalability across massive clusters. The benchmark validations indicate that our scheme is effective and accurate. Finally we would like to point out that our scheme has great potential in broad applications, such as fan noise analysis, etc.

References

- [1] L. Dong, S. T. Johansen, and T. A. Engh, Flow induced by an impeller in an UnBaffled tank-1, *Exp. Chem. Eng. Sci.*, 49(4) (1994), 549–560.
- [2] H. Hartmann, J. J. Derksen, C. Montavon, J. Pearson, I. S. Hamill, and H. E. A. Van Den Akker, Assessment of large eddy and RANS tank simulations by means of LDA, *Chem. Eng. Sci.*, 59 (2004), 2419–2432.
- [3] C. Y. Perng, and J. Y. Murthy, A moving deforming mesh technique for simulation of flow in mixing tanks, *A. IChE. Symp. Ser.*, 89(293) (1993), 37–41.
- [4] J. Y. Murthy, S. R. Mathur, and D. Choudahary, CFD simulation of flows in stirred tank reactors using a sliding mesh technique, *I. ChemE. Symp. Ser.*, 136 (1994), 341–348.
- [5] G. Tabor, A. D. Gosman, and R. Issa, Numerical simulation of the flow in a mixing vessel stirred by a rushton turbine, *I. ChemE. Symp. Ser.*, 140 (1996), 25–34.
- [6] Ph. Daskapoulous, and C. K. Harris, Three dimensional CFD simulations of turbulent flow in baffled stirred tanks, *I. ChemE. Symp. Ser.*, 140 (1996), 1–13.
- [7] S. Chen, and G. Doolen, Lattice Boltzmann method for fluid flows, *Ann. Rev. Fluid. Mech.*, 30 (1997), 329–364.
- [8] H. Chen, S. Chen, and W. Matthaeus, Recovery of the Navier-Stokes equations using a lattice-gas Boltzmann method, *Phys. Rev. A.*, 45 (1992), 5339–5342.
- [9] Y. H. Qian, D. d’Humières, and P. Lallemand, Lattice BGK models for Navier-Stokes equation, *Europhys. Lett.*, 17 (1992), 479–484.
- [10] X. Shan, X. F. Yuan, and H. Chen, Kinetic theory representation of hydrodynamics: a way beyond the Navier-Stokes equation, *J. Fluid. Mech.*, 550 (2006), 413–441.
- [11] R. Zhang, X. Shan, and H. Chen, Efficient kinetic method for fluid simulation beyond Navier-Stokes equation, *Phys. Rev. E.*, 74 (2006), 046703.
- [12] H. Chen, and X. Shan, Fundamental conditions for N -th order accurate lattice Boltzmann models, *Phys. D.*, 237(14) (2008), 2003–2008.
- [13] H. Chen, C. Teixeira, and K. Molvig, Realization of fluid boundary conditions via discrete Boltzmann dynamics, *Int. J. Mod. Phys. C.*, 9 (1998), 1281–1292.
- [14] X. Shan, and H. Chen, Lattice Boltzmann model for simulating flows with multiple phases and components, *Phys. Rev. E.*, 47 (1993), 1815–1819.

- [15] H. Chen, S. Kandasamy, S. Orszag, R. Shock, S. Succi, and V. Yakhot, Extended Boltzmann kinetic equation for turbulent flows, *Science*, 301 (2003), 633–636.
- [16] H. Chen, S. A. Orszag, I. Staroselsky, and S. Succi, Expanded analogy between Boltzmann theory of fluids and turbulence, *J. Fluid. Mech.*, 519 (2004), 301–314.
- [17] Y. Li, R. Shock, R. Zhang, and H. Chen, Numerical study of flow past an impulsively started cylinder by lattice Boltzmann method, *J. Fluid. Mech.*, 519 (2004), 273–300.
- [18] Y. Li, R. Shock, R. Zhang, and H. Chen, Simulation of flow over iced airfoil by using a lattice Boltzmann method, *AIAA Paper 2005-1103*, 43rd AIAA Aerospace Sciences Meeting and Exhibit, January 10-13, Reno, Nevada, 2005.
- [19] Z. Guo, C. Zhen, and B. Shi, Discrete lattice effects on the forcing term in the lattice Boltzmann method, *Phys. Rev. E.*, 65 (2002), 046308.
- [20] Y. Li, R. Zhang, R. Shock, and H. Chen, Prediction of vortex shedding from a circular cylinder using a volumetric Lattice-Boltzmann boundary approach, *Euro. Phys. J.*, 171 (2009), 91–97.
- [21] M. Pervaiz, and C. Teixeira, Two equation turbulence modeling with the lattice Boltzmann method, *Proceeding of ASME PVP Division Conference: 2nd International Symposium on Computational Technologies for Fluid/Thermal/Chemical Systems with Industrial Applications*, August, Boston, MA, USA, 1999.
- [22] S. D. Jessup, C. Schott, M. Jeffers, and S. Kobayashi, Local propeller blade flows in uniform and sheared onset flows using LDV techniques, *15th ONR Symposium on Naval Hydrodynamics*, Hamburg, Germany, 1984.
- [23] J. Jeong, and F. Hussain, On the identification of a vortex, *J. Fluid. Mech.*, 285 (1995), 69–94.